Available online at www.sciencedirect.com
SCIENCE DIRECT®
Corrosion Science 46 (2004) 1729–1739
CORROSION SCIENCE
www.elsevier.com/locate/corsci

Raman microscopy of chromate interactions with corroding aluminum alloy 2024-T3

Jeremy D. Ramsey, Richard L. McCreery *

Department of Chemistry, The Ohio State University, 100 W. 18th Avenue, Columbus, OH 43210, USA

Received 5 June 2003; accepted 15 October 2003
Available online 5 December 2003

Abstract

Raman microspectroscopy was used to observe actively corroding aluminum alloy 2024-T3 directly in a solution containing NaCl and dilute $K_2Cr_2O_7$. Raman spectra acquired in and near corrosion pits allowed identification of two products of Cr^{VI} interactions with the corroding alloy. If the alloy potential was fixed negative of the pitting potential, an Al^{III}–Cr^{VI} mixed oxide formed in formerly active or metastable pits. This mixed oxide is similar to a covalent compound which can be made synthetically by adding NaOH to solutions containing Al^{3+} and CrO_4^{2-}. If the alloy potential was held positive of the pitting potential, the corrosion product was primarily a Cr^{III}–Cr^{VI} mixed oxide, formed by partial reduction of Cr^{VI} to Cr^{III} by exposed Al metal or by H_2. At the pitting potential, a mixture of Al^{III} and Cr^{III} mixed oxides was observed, with the Al^{III} species located primarily within pits. A model for the formation mechanism of the mixed oxides is proposed, and the consequences of the findings to corrosion inhibition by Cr^{VI} are considered. In particular, the concentration of Cr^{VI} in and near pits driven by mixed oxide formation may serve to direct the inhibitor from the solution to sites of corrosion.

1. Introduction

Hexavalent chromium has a number of inhibitory effects on aluminum and its alloys. The properties most commonly attributed to Cr^{VI} as an inhibitor are the healing of flaw sites in anodic films [1], neutralization of surface charge [2–6], and

* Corresponding author. Tel.: +1-614-292-2021; fax: +1-614-688-5402.
E-mail address: mccreery.2@osu.edu (R.L. McCreery).

0010-938X/$ - see front matter © 2003 Elsevier Ltd. All rights reserved.
doi:10.1016/j.corsci.2003.10.010

retardation of oxygen reduction kinetics [7–10]. Although the effectiveness of Cr^{VI} as an inhibitor of aluminum alloy corrosion is unmatched, Cr^{VI} has extreme effects on ecosystems. It is highly toxic and has been determined to have carcinogenic activities [11]. Because of this, replacements for Cr^{VI} are being sought in a number of industries, but most notably in the aerospace industry [12,13].

The search for environmentally benign alternatives to chromate-based corrosion inhibitors has resulted in a surge of interest in the mechanism of chromate protection. If the mechanism of the excellent protection afforded by chromate conversion coatings (CCC) and chromate containing primers were understood, effective substitutes could be rationally designed. Several observations about chromate protection of aluminum alloys are relevant to the current work: first, CCCs consist of both Cr^{III} and Cr^{VI} in the form of amorphous mixed oxides [14–16]. Second, Cr^{VI} is released from a CCC into aqueous surface films or bulk solution, to a level of approximately 10^{-4} M [16,17]. Third, Cr^{VI} in solution, usually as CrO_4^{2-} or $HCrO_4^-$, can diffuse to defects or damage locations and protect them from further corrosion [17]. In this sense, CCCs and chromate containing pigment ($SrCrO_4$, etc.) both act as storage reservoirs for soluble Cr^{VI} species. The combination of storage, release, and migration of Cr^{VI} is responsible for the important "self-healing" action of chromate containing coatings. Fourth, Cr^{VI} appears to inhibit both O_2 reduction and anodic dissolution of intermetallic particles in aluminum/copper alloys such as aluminum alloy 2024-T3 (AA2024-T3) [10]. It is not clear whether CrO_4^{2-}, $HCrO_4^-$ or a Cr^{VI} reduction product is the active inhibitor, but there is strong support for the importance of Cr^{VI} mobility in providing self-healing.

Previous reports have established that dilute Cr^{VI} protects AA2024-T3 alloy from corrosion, implying that the other agents in the CCC formulation (F^-, $Fe(CN)_6^{3-}$) or pigment (Sr^{2+}) are not necessary for corrosion protection by the coating system [17]. If dilute Cr^{VI} provides corrosion protection, whether or not it originated as a CCC or as $SrCrO_4$, the major question of how dilute Cr^{VI} interacts with AA2024-T3 alloy remains. Such an interaction must be involved in the inhibition mechanism, whether Cr^{VI} acts as an anodic, cathodic, or mixed inhibitor. Past efforts have shown that Cr^{VI} is deposited on AA2024-T3 surfaces in the form of an Al^{III}–Cr^{VI} mixed oxide, and this deposit was concentrated near corrosion sites, pits and/or intermetallic compounds (IMC's), on the alloy surface [18,19]. We report herein a more detailed investigation of Cr^{VI} interactions with pits and IMC's on AA2024-T3. Raman microscopy and imaging were used to identify localized Cr^{VI} products following immersion of AA2024-T3 alloy in $K_2Cr_2O_7$ solutions containing chloride ion.

2. Experimental

Reagents and alloy samples were acquired and prepared as described previously [18] but with some minor modifications. All solutions were prepared using Nanopure water (Barnstead) with a minimum resistivity of 18 MΩ, and reagents were used as received. In most cases, epoxy mounted AA2024-T3 samples were polished with silicon carbide paper in water to a grit size of 1200. Intermetallic particles were more

easily observed with a finer polish, so a few alloy samples were subsequently polished using 0.3 μm alumina slurries in water. Although polishing in water is known to lead to dealloying in some cases [20], water polishing was used here to avoid possible spectroscopic contamination caused by residual organic molecules. Synthetic mixed oxides of Cr^{VI} were prepared through precipitation by adding 1 M NaOH dropwise to a solution of the appropriate metal salt (e.g. Al^{III}, Cr^{III}, Fe^{III}, Cu^{II}, Mg^{II}) and $K_2Cr_2O_7$. In all cases, the initial molar ratio of the metal ion to Cr^{VI} concentration in solution was 3:1, typically 0.2 M metal cation and 0.03 M $K_2Cr_2O_7$. The solid mixed oxides were collected by vacuum filtration following observation of a precipitate ($pH > 4$; dependent on metal ion). In this work, collection predominantly occurred above pH 6. In the case of Al^{III}–Cr^{VI} mixed oxide, the pH at the point of collection varied, as indicated in text and figures.

Mounted and polished alloy samples were prepared for Raman examination by open circuit or potentiostatic exposure to 0.1 M NaCl solution containing Cr^{VI}. Using a Gamry PC 3–300 potentiostat, the potential was held at various values relative to the open circuit for a period of 15 min in aerated solutions of 0.1 M NaCl containing 40 or 80 mM Cr^{VI} (concentrations refer to total Cr^{VI} in solution, unless indicated otherwise). Depending on the applied potential, various degrees of corrosion were observed. The sample was subsequently removed from solution and rinsed thoroughly with water. Raman spectroscopy was performed using a Dilor X-Y imaging spectrometer with a 40× water immersion microscope objective (Olympus). The sample was submerged in Nanopure water during the entire Raman signal acquisition to minimize sample heating. Raman images were collected while the laser beam was rastered across a line on the sample while a translation stage was stepped along an orthogonal axis. The end result was a collection of Raman spectra acquired as a grid on the sample surface with a typical grid density of 40×50 Raman spectra, which typically covered a 160×200 μm region of the alloy surface. Raman spectra of bulk synthetic mixed oxides were obtained using the same spectrometer in macro-sampling mode, for which the laser spot size was approximately 50 μm.

3. Results

Fig. 1 shows reference spectra for several materials that are relevant to the current work. The Raman bands in the 800–900 cm^{-1} region are derived from the Cr–O stretch of the $Cr^{VI}O_4$ tetrahedron, which are perturbed by interaction with the various metal oxides. Although the spectra of both Cr^{III}–Cr^{VI} and Al^{III}–Cr^{VI} mixed oxides have similar features, there are important differences that allow spectral identification. The primary Cr^{III}–Cr^{VI} mixed oxide Raman feature is centered at 860 cm^{-1} with pH-independent shape and position. Fig. 1 shows two different Al^{III}–Cr^{VI} mixed oxides, collected at pH 7.6 and 4.25, revealing that at least three bands comprise the Al^{III}–Cr^{VI} mixed oxide spectrum. The details of the Al^{III}–Cr^{VI} and Cr^{III}–Cr^{VI} spectra have been discussed previously, [14,18,19] but the peak position and shape are used herein to permit discrimination of chromium and aluminum mixed oxides. Mixed oxides of Cr^{VI} were also prepared by precipitation of Mg^{II},

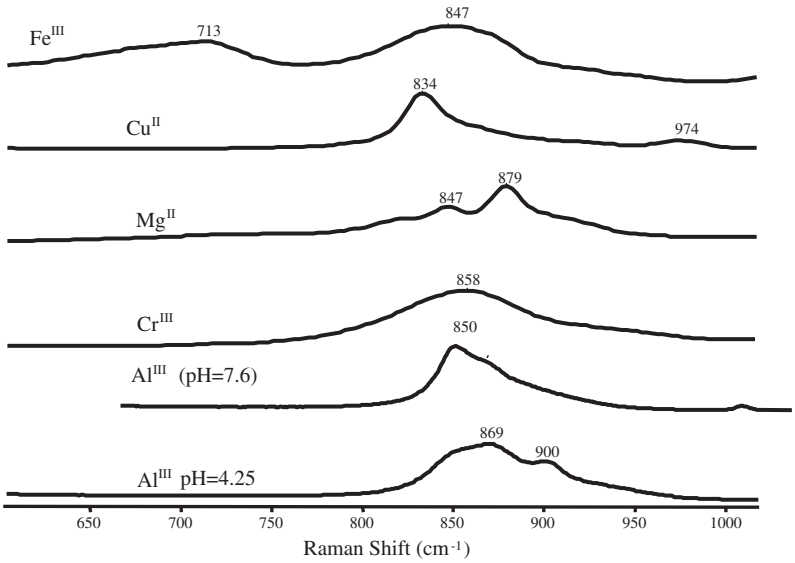

Fig. 1. Raman spectra of synthetic metal–Cr^{VI} mixed oxides formed by addition of NaOH to a solution of the indicated metal ion and Cr^{VI}. The pH of collection for Al^{III}–Cr^{VI} mixed oxide spectra is indicated since its spectrum varies significantly with collection conditions.

Cu^{II}, and Fe^{III} metal ions from Cr^{VI} solution in a manner similar to that described previously for Al^{III}–Cr^{VI} and Cr^{III}–Cr^{VI} [14,18,19]. The spectra shown in Fig. 1 demonstrate that the Al^{III}, Cr^{III}, Cu^{II}, Mg^{II} and Fe^{III} mixed oxides all have Raman features in the region of 850 cm^{-1}, however, the peak position and peak shape vary significantly with the identity of the metal ion. In particular, note that the Cu^{II}, Mg^{II} and Fe^{III} mixed oxides have different peak frequencies and peak structures when compared to the Cr^{III}–Cr^{VI} and Al^{III}–Cr^{VI} mixed oxides. These differences allow for identification of the species on corroding surfaces exposed to Cr^{VI}.

The interactions of dilute Cr^{VI} with various surface features on AA2024-T3 were examined by exposing a pretreated alloy surface to dilute chromate solution. Fig. 2 shows a polarization curve for AA2024 alloy in Cr^{VI} solution with the indicated potentials corresponding to subsequently indicated figures. The open circuit potential varied somewhat with pretreatment but was generally between −550 and −570 mV versus Ag/AgCl, and pitting proceeded above −410 mV versus Ag/AgCl. Fig. 3 illustrates the case of an alloy surface held below the pitting potential in a solution of NaCl and Cr^{VI}. The small pit apparent in the video micrograph was probed with Raman spectroscopy to yield the series of spectra shown in the three-dimensional plot. The Raman scattering in the 800–900 cm^{-1} region was centered at 851 cm^{-1}, and was most intense inside the pit. Based on visual observation, the feature appears to be a formerly active pit. Fig. 4 shows an example of an extensively corroded sample, which had been held above the pitting potential for 15 min in chloride solution containing Cr^{VI}. The video micrograph shows extensive localized corrosion

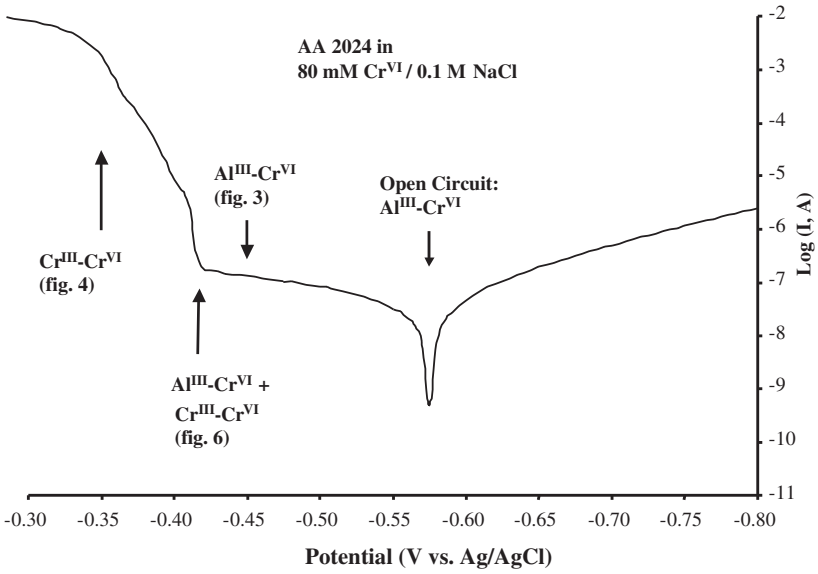

Fig. 2. Polarization curve of AA2024-T3 in a 0.08 M Cr^{VI}/0.1 M NaCl solution (pH 5). The alloy sample had an exposed area of 1 cm^2. Labels along curve indicate the potentials at which subsequent spectra were obtained, and the primary corrosion product observed at that potential.

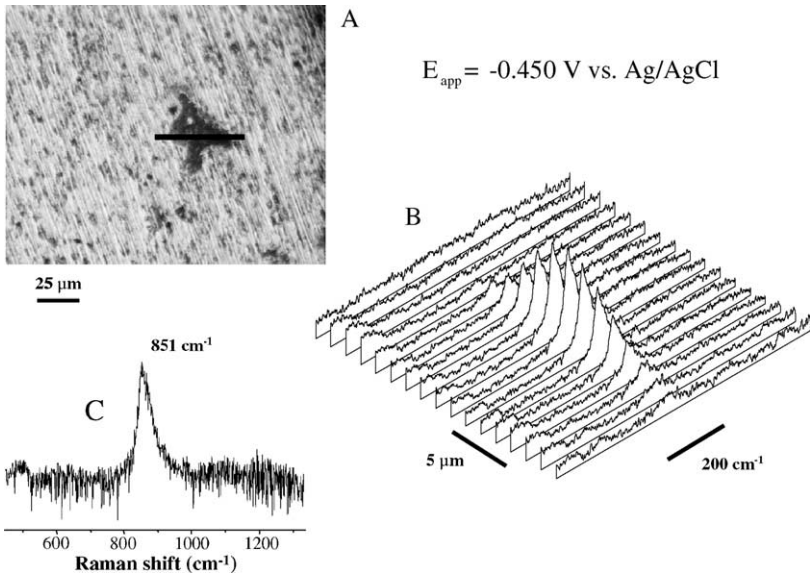

Fig. 3. Raman profile across a pit from an AA2024 sample polarized at −0.450 V versus Ag/AgCl in a 0.04 M Cr^{VI}/0.1 M NaCl solution: (A) video micrograph of the surface, (B) Raman profile acquired over the line indicated on the micrograph, with beam translated 1 μm between spectra, (C) single Raman spectrum taken from (B).

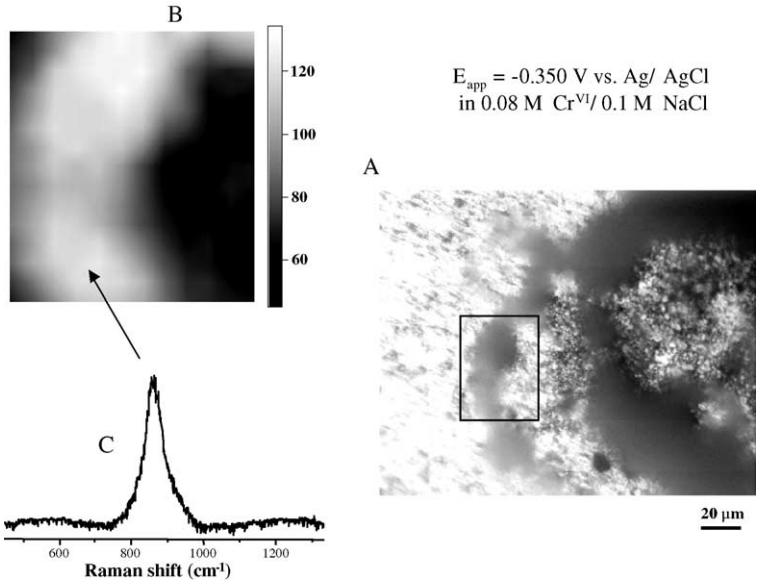

Fig. 4. Raman image of a precipitated product on the AA2024 surface following polarization at −0.350 V in 0.08 M Cr^{VI}/0.1 M NaCl solution: (A) video micrograph of the surface, (B) Raman image of the region indicated by a box on the video micrograph, with lighter shade indicating higher Raman intensity, (C) Raman spectrum of the corrosion product. The units shown with the gray scale are proportional to scattered light intensity, but are otherwise arbitary.

and Raman spectra of the affected region show a peak centered at 860 cm^{-1}. The 860 cm^{-1} band appeared over an extensive region surrounding what appeared to be a large pit. Raman spectra from Figs. 3 and 4 are compared in Fig. 5 with those of synthetic mixed oxides. There is a small but definite difference between the spectra obtained on alloy surfaces above and below the pitting potential. Both the peak center and peak shape indicate that the corrosion product formed below the pitting potential is primarily Al^{III}–Cr^{VI} mixed oxide, whereas the product formed above the pitting potential is primarily Cr^{III}–Cr^{VI} mixed oxide. Fig. 6 shows Raman spectral images from a sample held at the pitting potential. The region within the white box of the video micrograph was analyzed using a 39×46 spatial grid with a complete Raman spectrum acquired at each of the 1794 grid positions. The spectral analysis software permitted the creation of intensity maps showing the contribution of either the Al^{III} or the Cr^{III} mixed oxide spectra to the observed spectra. The resulting intensity maps show the distribution of Al^{III}–Cr^{VI} and Cr^{III}–Cr^{VI} mixed oxide within the white box. The highest concentration of Al^{III} mixed oxide is within the pit shown in the video micrograph, while Cr^{III} mixed oxide was found both in and around the same pit.

It is also important to understand the interaction of Cr^{VI} with intermetallic sites as they are thought to be sites of cathodic activity [21–27]. The size of these particles precludes the use of macro-Raman systems as was previously demonstrated with pitting sites [18] and necessitates the use of a micro-Raman system that utilizes a

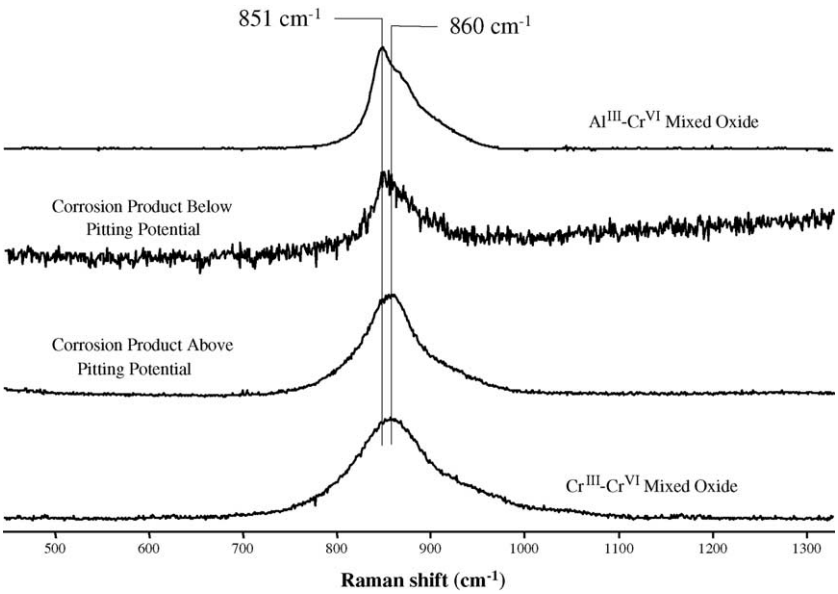

Fig. 5. Raman spectra of corrosion products observed on alloy surfaces following exposure to Cr^{VI} solutions under potential control. Relevant spectra of synthetic reference materials (Al^{III}–Cr^{VI} and Cr^{III}–Cr^{VI} mixed oxides) are shown for comparison.

laser spot size on the order of the intermetallic particle diameter. However, attempts at monitoring in situ interactions between Cr^{VI} and intermetallic surfaces were frustrated by photo-reduction due to high laser power density, which is common with microscopic Raman techniques. In all cases, Cr^{III}–Cr^{VI} was observed in the entire area illuminated by the laser spot and occurred even on pure aluminum samples. No correlation between the formation of Cr^{III}–Cr^{VI} mixed oxide and intermetallic particles or other surface features could be established.

4. Discussion

Although the Raman spectra of Fig. 1 were used herein mainly as ''fingerprints'' for particular mixed oxides, some comments about the appearance of the spectra are useful. Raman and infrared spectra of Cr^{VI} in aqueous solution have been previously assigned [28–35]. The spectra contain well defined, narrow (10–20 cm^{-1} FWHM) bands in the 800–950 cm^{-1} region for CrO_4^{2-} (847 cm^{-1}), $HCrO_4^-$ (898 cm^{-1}), and $Cr_2O_7^{2-}$ (904 cm^{-1}), with the frequencies similar to the sharp bands observed in ionic salts such as K_2CrO_4 (853 cm^{-1}, <10 cm^{-1} FWHM) and $K_2Cr_2O_7$ (911 cm^{-1}, ~10 cm^{-1} FWHM). The larger bandwidths (30–50 cm^{-1}) and changes in band structure apparent in the mixed oxide spectra (Fig. 1) indicate a strong interaction between the metal ions and the Cr^{VI} oxide tetrahedron. As discussed elsewhere, it is more

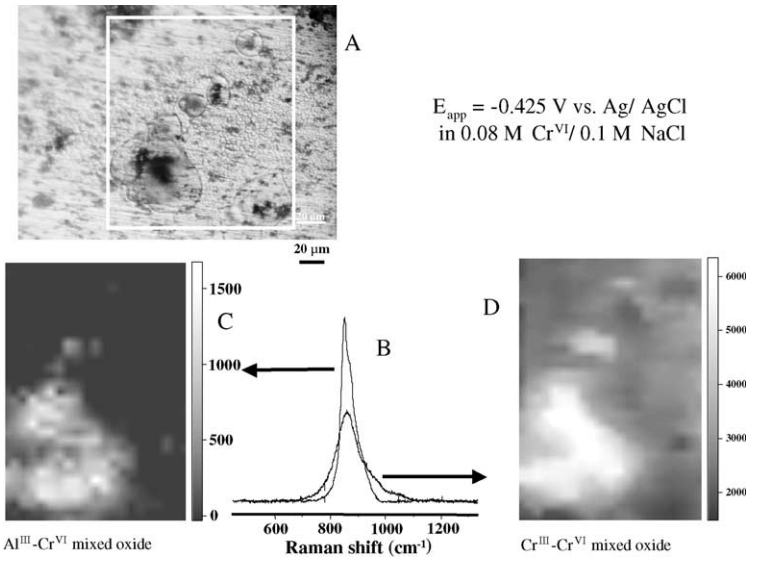

Fig. 6. Raman image of an AA2024 surface region following polarization at −0.425 V in 0.08 M Cr^{VI}/0.1 M NaCl solution: (A) video micrograph of the surface, (B) Raman spectra of reference mixed oxides, (C) Raman image, with lighter color indicating the intensity of the 851 cm^{-1} Al^{III}–Cr^{VI} mixed oxide, and (D) Raman image of the intensity of the 860 cm^{-1} Cr^{III}–Cr^{VI} mixed oxide band. The two images were deconvoluted from one data set using the reference spectra in (B) and a principal component analysis tool contained in the Dilor software. The units shown with the gray scale are proportional to scattered light intensity, but are otherwise arbitary.

accurate to consider the mixed oxides to be covalent, polymeric compounds rather than ionic salts [14–16,18,19]. Although the formation of the mixed oxides resembles an adsorption process and is reversible [16], there is strong evidence for the existence of a covalent M–O–Cr^{VI} bond, which accounts for the strong perturbation of the Cr^{VI} Raman features in the mixed oxides [14–19].

Unfortunately, Cr^{III} and Al^{III} oxides are significantly weaker Raman scatterers than Cr^{VI}, and were not detectable on alloy surfaces under the current experimental conditions. The Cr^{VI} center is preresonantly enhanced at 514.5 mm, so the Raman detection limits for Cr^{VI} and its compounds are significantly lower than those for Cr^{III} or Al^{III} oxides in the absence of Cr^{VI}. Consequently, appreciable levels of Cr^{III}, Al^{III}, Cu^{II}, Fe^{III}, and Mg^{II} oxides were present on corroding AA2024 but were not detected unless they interacted with Cr^{VI}. Conversely, the absence of Raman features attributable to Mg^{II}–Cr^{VI}, Cu^{II}–Cr^{VI} and Fe^{III}–Cr^{VI} mixed oxides implies they are absent or occur at very low levels.

The Raman spectra and images shown in Figs. 3–6 demonstrate that different products are formed when solution phase Cr^{VI} encounters corrosion sites in AA2024 at potentials above or below the pitting potential (E_{pit}). As indicated on the polarization curve of Fig. 2, the Al^{III}–Cr^{VI} mixed oxide forms predominately at potentials negative of E_{pit}, with the highest concentration observed at corrosion sites. At

potentials above E_{pit}, the Cr^{III}–Cr^{VI} mixed oxide predominates, and is distributed near and around an active pit. When the potential is controlled at E_{pit}, both Al^{III} and Cr^{III} mixed oxides are observed, with the Al^{III}–Cr^{VI} oxide in the pit and Cr^{III}–Cr^{VI} oxide scattered over a larger area. The sequence of steps implied by the results shown in Fig. 3 is straightforward and results in the observed deposit of Al^{III}–Cr^{VI} mixed oxide. Below E_{pit}, a pit is at best metastable, and a formerly active pit will contain $Al^{III}(OH)_x$ formed from Al^{3+} hydrolysis. After hydrolysis of Al^{3+} the pH in and near the pit will slowly increase after the pit becomes inactive. The $Al^{III}(OH)_x$ precipitate reacts with Cr^{VI} from solution to form the Al^{III}–Cr^{VI} mixed oxide, which remains inside or very close to the pit. As shown in Fig. 3, the mixed oxide formed at potentials negative of E_{pit} has the 851 cm^{-1} peak maximum characteristic of the Al^{III}–Cr^{VI} mixed oxide.

Above the pitting potential (Fig. 4), the situation is more complicated due to H_2 evolution and active corrosion during mixed oxide formation. The predominance of Cr^{III}–Cr^{VI} mixed oxide with its characteristic 860 cm^{-1} Raman frequency obviously requires that Cr^{VI} is reduced, presumably by the bare Al^{III} surface at the pit wall or by H_2 evolved at actively growing pits. As shown schematically in Fig. 7, $Cr^{III}(OH)_x$ formed by reduction is likely to be concentrated in the active pit, but is subsequently driven out by H_2 bubbles. The result is Cr^{III}–Cr^{VI} mixed oxide scattered around the periphery of the pit. Note that the reaction between Cr^{III} and solution phase Cr^{VI} to form mixed oxide may occur within the pit before expulsion or around the pit following expulsion. It is clear, however, that Cr^{VI} adsorbs to $Cr^{III}(OH)_x$, regardless of its origin or location.

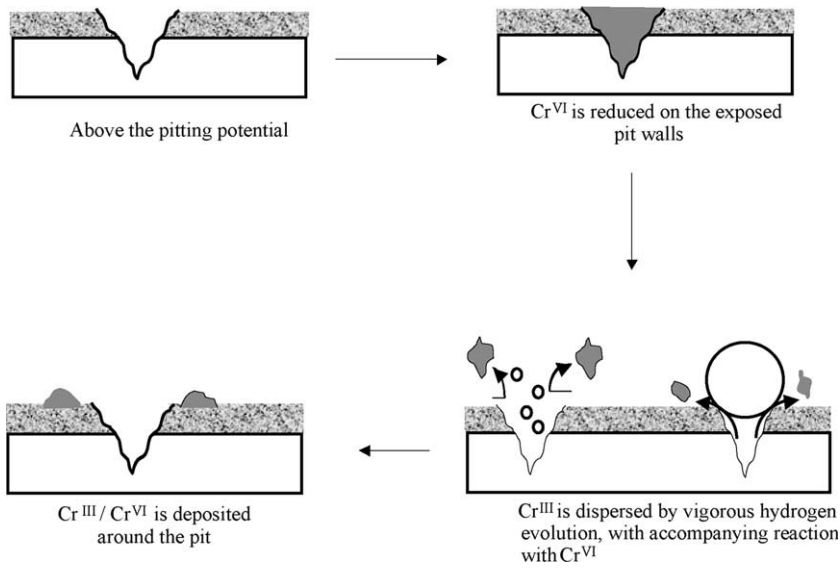

Fig. 7. Proposed mechanism of the interaction of Cr^{VI} with an aluminum alloy surface above the pitting potential. Relatively high Cr^{III} concentration in active pit permits formation of Cr^{III}–Cr^{VI} mixed oxide.

It is important to note that the band shape and frequency of the Al^{III}–Cr^{VI} mixed oxide Raman spectrum observed in this study as well as previously reported [18,19], implies that the formation pH was well above pH 7. This may be due to the deposition area having an elevated pH expected near cathodic sites. O_2 reduction causes the pH to increase locally, with at least two possible consequences. First, a high pH would destabilize the $Al(OH)_x$ on the matrix around the IMC particle, thus exposing Al metal and accelerating corrosion. Second, the higher pH would explain the shape of the Al^{III}–Cr^{VI} mixed oxide band observed on AA2024 surfaces. The correspondence of the spectrum to that for synthetic Al^{III}–Cr^{VI} mixed oxide collected at pH 7.6 implies either that the local pH during corrosion was slightly basic, consistent with a cathodic site, or that the acidity associated with Al^{3+} hydrolysis had dissipated prior to Cr^{VI} adsorption.

The implication of the current findings to the corrosion inhibition mechanism of Cr^{VI} depends on the primary locus of chromate activity. The distribution of Cr^{VI} shown in Figs. 3, 4, and 6 clearly demonstrates that the highest concentrations of adsorbed Cr^{VI} are in and near pits, which are themselves often associated with $Al_2(CuFeMn)$ particles. Since both pits and IMC's are involved in AA2024 corrosion, the local formation of Al^{III} and Cr^{III} mixed oxides serves to direct the inhibitor to the actively corroding regions. If Cr^{VI} protects primarily by cathodic inhibition, the concentration of Cr^{VI} near intermetallic particles should be important. If Cr^{VI} also acts as an anodic inhibitor, its concentration in pits should be advantageous. On both pits and IMC particles, the process of concentrating of Cr^{VI} is driven by formation of either Al^{III} or Cr^{III} mixed oxide.

The observation of Cr^{III}–Cr^{VI} mixed oxide on AA2024 samples held above the pitting potential in Cr^{VI} solution is direct evidence for the reduction of Cr^{VI} to Cr^{III}. Cr^{VI} reduction is not surprising, since it occurs on a much larger scale during CCC formation in Alodine 1200S and related treatment baths. In a CCC, the Cr^{III}–Cr^{VI} mixed alloy stores Cr^{VI} for later release, and the Cr^{III} mixed oxide observed in Fig. 5 may serve the same function on a smaller scale. The connection between Cr^{VI} reduction on AA2024 under field conditions and the inhibition of O_2 reduction is currently under examination.

Acknowledgements

This work was supported by the Air Force Office of Scientific Research via the Multidisciplinary University Research Initiative, and by the Strategic Environmental Research & Development Program. The authors acknowledge useful conversations with Gerald Frankel, R.G. Buchheit, and Martin Kendig.

References

[1] J.K. Hawkins, H.S. Isaacs, S.M. Heald, J. Tranquada, G.E. Thompson, G.C. Wood, Corros. Sci. 27 (4) (1987) 391–399.
[2] S. Matsuda, H.H. Uhlig, J. Electrochem. Soc. 111 (2) (1964) 156–161.

[3] M.A. Heine, M.J. Pryor, J. Electrochem. Soc. 144 (10) (1967) 1001–1006.
[4] E. McCafferty, J. Electrochem. Soc. 137 (12) (1990) 3731–3737.
[5] C.B. Breslin, G. Treacy, W.M. Carroll, Corros. Sci. 36 (7) (1994) 1143–1154.
[6] M.W. Kendig, R. Addison, S. Jeanjaquet, J. Electrochem. Soc. 146 (12) (1999) 4419.
[7] I.M. Kolthoff, A.M. Shams El Din, J. Phys. Chem. 60 (1956) 1564–1568.
[8] G. Lindbergh, D. Simonsson, Electrochim. Acta 36 (13) (1991) 1985–1994.
[9] A.E. Hughes, C.M. Haas, Surf. Interface Anal. 21 (1994) 65–78.
[10] W.J. Clark, J.D. Ramsey, R.L. McCreery, G.S. Frankel, J. Electrochem. Soc. 149 (5) (2002) B179–B185.
[11] S.A. Katz, H. Salem, The Biological and Environmental Chemistry of Chromium, VCH Publishers, New York, 1994, pp. 65–119.
[12] E. Greshart, Metal Finish. (Mar.) (1997) 59–61.
[13] R.L. Twite, G.P. Bierwagen, Prog. Org. Coat. 33 (1998) 91–100.
[14] L. Xia, R.L. McCreery, J. Electrochem. Soc. 145 (9) (1998) 3083–3089.
[15] L. Xia, R.L. McCreery, J. Electrochem. Soc. 146 (10) (1999) 3696–3701.
[16] L. Xia, E. Akiyama, G.S. Frankel, R.L. McCreery, J. Electrochem. Soc. 147 (7) (2000) 2556.
[17] J. Zhao, G.S. Frankel, R.L. McCreery, J. Electrochem. Soc. 145 (7) (1998) 2558.
[18] J.D. Ramsey, R.L. McCreery, J. Electrochem. Soc. 146 (11) (1999) 4076–4081.
[19] J.D. Ramsey, The corrosion inhibition mechanism of chromium(VI): probing the interaction of chromium(VI) with aluminum alloy surfaces. Ph.D. Thesis, The Ohio State University, Columbus, OH, March 2001.
[20] R.G. Buchheit, R.P. Grant, P.F. Hlava, B. McKenzie, G.L. Zender, J. Electrochem. Soc. 144 (8) (1997) 2621–2628.
[21] H. Bohni, H.H. Uhlig, J. Electrochem. Soc. 116 (7) (1969) 906–910.
[22] M.A. Alodan, W.H. Smyrl, J. Electrochem. Soc. 144 (10) (1997) L282–L284.
[23] M.A. Alodab, W.H. Smyrl, J. Electrochem. Soc. 145 (5) (1998) 1571–1577.
[24] J.O. Park, C.H. Paik, Y.H. Huang, R.C. Alkire, J. Electrochem. Soc. 146 (2) (1999) 517–523.
[25] R.G. Buchheit, L.P. Montes, M.A. Martinez, J. Michael, P.F. Hlava, J. Electrochem. Soc. 146 (12) (1999) 4424–4428.
[26] M. Buchler, J. Kerimo, F. Guillaume, W.H. Smyrl, J. Electrochem. Soc. 147 (10) (2000) 3691–3699.
[27] M. Buchler, T. Watani, W.H. Smyrl, Corros. Sci. 42 (2000) 1661–1668.
[28] H. Stammreich, D. Bassi, D. Sala, H. Siebert, Spectrochim. Acta 13 (1958) 192.
[29] D.A. Brown, D. Cunningham, W.K. Glass, Spectrochim. Acta 24A (1968) 965–968.
[30] I.R. Beattie, T.R. Gilson, J. Chem. Soc. A (1970) 980–986.
[31] D.M. Adams, M.A. Hooper, M.H. Lloyd, J. Chem. Soc. A (1971) 946–947.
[32] J.E.D. Davies, D.A. Long, J. Chem. Soc. A (1971) 1275.
[33] N. Weinstock, H. Schulze, A.J. Mueller, J. Chem. Phys. 59 (9) (1973) 5063.
[34] J.D. Ramsey, L. Xia, M.W. Kendig, R.L. McCreery, Corros. Sci. 43 (2001) 1557–1572.
[35] M.M. Hoffmann, J.G. Darab, J.L. Fulton, J. Phys. Chem. A 105 (2001) 1772–1782.